Constraints on the star formation histories of galaxies from $z \sim 1$ **to** $z \sim 0$

Yan-Mei Chen[1,2]⋆, Vivienne Wild[2], Guinevere Kauffmann[2], Jérémy Blaizot[3], Marc Davis[4,5], Kai Noeske[6], Jian-Min Wang[1,7], Christopher Willmer[8]

[1] *Key Laboratory for Particle Astrophysics, Institute of High Energy Physics, Chinese Academy of Sciences, 19B Yuquan Road, Beijing 100049, China*
[2] *Max–Planck–Institut für Astrophysik, Karl–Schwarzschild–Str. 1, D-85748 Garching, Germany*
[3] *Université de Lyon, Lyon, F-69003; Université Lyon 1, Observatoire de Lyon, 9 avenue Charles André, Saint-Genis Laval, F-69230; CNRS, UMR 5574, Centre de Recherche Astrophysique de Lyon; Ecole Normale Supérieure de Lyon, Lyon, F-69007, France*
[4] *Department of Astronomy, University of California, Berkeley, CA 94720, USA*
[5] *Department of Physics, University of California, Berkeley, CA 94720, USA*
[6] *W. M. Keck Postdoctoral Fellow at the Harvard-Smithsonian Center for Astrophysics, 60 Garden St, Cambridge, MA 02138, USA*
[7] *Theoretical Physics Center for Science Facilities, Chinese Academy of Sciences, China*
[8] *Steward Observatory, University of Arizona, 933 N Cherry Ave, Tucson, AZ 85721, USA*

19 November 2008

ABSTRACT
We present a new method to estimate the average star formation rate per unit stellar mass (SSFR) of a stacked population of galaxies. We combine the spectra of $600-1000$ galaxies with similar stellar masses and parameterise the star formation history of this stacked population using a set of exponentially declining functions. The strength of the Hydrogen Balmer absorption line series in the rest-frame wavelength range $3750-4150$Å is used to constrain the SSFR by comparing with a library of models generated using the BC03 stellar population code. Our method, based on a principal component analysis (PCA), can be applied in a consistent way to spectra drawn from local galaxy surveys and from surveys at $z \sim 1$, and is only weakly influenced by attenuation due to dust. We apply our method to galaxy samples drawn from SDSS and DEEP2 to study mass-dependent growth of galaxies from $z \sim 1$ to $z \sim 0$. We find that, (1) high mass galaxies have lower SSFRs than low mass galaxies; (2) the average SSFR has decreased from $z = 1$ to $z = 0$ by a factor of $\sim 3-4$, independent of galaxy mass. Additionally, at $z \sim 1$ our average SSFRs are a factor of $2-2.5$ lower than those derived from multi-wavelength photometry using similar datasets. We then compute the average time (in units of the Hubble time, $t_{\rm H}(z)$) needed by galaxies of a given mass to form their stars at their current rate. At both $z = 0$ and at $z = 1$, this timescale decreases strongly with stellar mass from values close to unity for galaxies with masses $\sim 10^{10} M_\odot$, to more than ten for galaxies more massive than $10^{11} M_\odot$. Our results are in good agreement with models in which AGN feedback is more efficient at preventing gas from cooling and forming stars in high mass galaxies.

Key words: galaxies: evolution – galaxies: star formation

1 INTRODUCTION

Over the last decade, there have been a large number of photometric and spectroscopic surveys designed to study the formation and evolution of galaxies. One major conclusion of these studies has been that the epoch when massive galaxies formed most of their stellar mass is significantly earlier than that for low mass galaxies (Heavens et al. 2004; Thomas et al. 2005). This phenomenon, popularly known as "down-sizing", at first sight seems at odds with the predictions of the hierarchical CDM model, in which dark matter halos of all masses grow through merging and accretion right up to the present day. The only way to reconcile the observations with the theory, is to postulate that the growth of the most massive galaxies is much slower than the growth of their surrounding halos.

⋆ Email: chenym@mail.ihep.ac.cn

The most natural way to achieve this is by invoking feedback processes, which prevent gas from cooling, condensing and forming stars in massive halos (Bower et al. 2006; Croton et al. 2006; De Lucia et al. 2006; Guo & White 2008). A variety of different feedback mechanisms have been included in numerical and semi-analytic models, for example feedback from quasars and radio AGN (Silk & Rees 1998; Hopkins et al. 2006; Wang et al. 2006, 2007), supernova heating (Cole et al. 2000; Benson et al. 2003; Stringer et al. 2008) and heating by infalling substructure (Dekel & Birnboim 2008). A physical understanding of feedback is still lacking, however, and it is not understood which, if any, of the proposed mechanisms are most important in regulating the growth of galaxies. It is likely that each mechanism will come into play at a different mass scale and cosmological epoch. By quantifying in detail how galaxies of different masses grow as a function of time, we hope to clarify how different galaxies form their stars and how this is influenced by feedback processes.

There have been many attempts to measure the star formation rates of galaxy populations from the present day out to redshifts greater than 5 (see for example Brinchmann et al. 2004; Bauer et al. 2005; Feulner et al. 2005; Noeske et al. 2007a). For nearby galaxies, the Hα line provides the most reliable estimate of SFR, since it directly measures the number of ionizing photons from massive stars. A reasonably reliable correction for dust extinction can be made provided one also measures the Balmer decrement Hα/Hβ accounting accurately for stellar absorption. Beyond redshifts of ~ 0.4, the Hα redshifts out of the optical part of the spectrum and is no longer accessible. [O II] equivalent widths, ultraviolet (UV)-optical spectral energy distribution (SED) fitting and infrared photometry are commonly used to estimate the star formation rate. Each of these indicators is subject to different disadvantages. The [O II] equivalent width is strongly affected by dust and by metallicity. The UV luminosities of galaxies are also strongly affected by dust, while the infrared only provides a direct measure of SFR if one has measurements across the thermal peak of the spectrum. This has not been the case for many of the Spitzer surveys aimed at quantifying star formation in high-redshift galaxies. All the indicators discussed above may also be contaminated by AGN emission if there is an actively accreting black hole in the galaxy.

In this paper, we develop an approach to estimate the amount of recent star formation experienced by a *population* of galaxies. Our method is based on the Balmer absorption lines located in the rest-frame wavelength range $3750 - 4150$Å of the galaxy spectrum. The advantages of our method are the following:

(1) The Balmer absorption lines are weakly influenced by dust attenuation and AGN contamination compared with the indicators discussed above.

(2) The wavelength range spanned by the Balmer absorption lines is accessible out to redshifts greater than 1, even in optical spectra. This means that the method can be applied in a consistent manner to both low and high redshift ($z \sim 1$) samples.

(3) By stacking a large number of galaxies, we estimate SFRs for a *complete sample* of galaxies in a given stellar mass range, including those galaxies that are forming stars

weakly or not at all. These galaxies are often excluded when SFRs are measured for individual objects.

We apply our method to a large sample of galaxy spectra from the Sloan Digital Sky Survey (SDSS) and the DEEP2 redshift survey to study the evolution of galaxies from $z = 1$ to $z = 0$. This redshift interval accounts for roughly half the age of the universe. Our study thus addresses the final stage of galaxy build-up in the Universe.

This paper is arranged as follows. In §2, we introduce the SDSS and DEEP2 samples used in our studies. The method to estimate the amount of recent star formation in our galaxies is developed in §3. We apply the method to the SDSS and DEEP2 samples, and present our results in §4 and §5, respectively. A discussion of the results is given in §6. §7 contains the summary of the paper. We use the cosmological parameters $H_0 = 70$ km s^{-1} Mpc^{-1}, $\Omega_{\mathrm{M}} = 0.3$ and $\Omega_{\Lambda} = 0.7$ throughout this paper.

2   SAMPLE SELECTION

2.1   The SDSS galaxy sample

The low redshift galaxy sample comes from data release 4 (DR4, Adelman-McCarthy et al. 2006) of the SDSS, which contains more than 550000 spectra in the primary redshift range $0 \leqslant z \leqslant 0.3$. Stellar masses of the galaxies are obtained by fitting a suite of BC03 models (described in Salim et al. 2007) to the SDSS model magnitudes. These masses are not identical to those of Kauffmann et al. (2003) or Gallazzi et al. (2005), who use spectral indices, such as the D4000 and Hδ_{A} to constrain the mass-to-light ratios of the galaxies. However, the differences between the mass estimates are very small, the median offset of $\log M_*$ is only 0.01. In this work we choose to use the photometric masses in order to maintain consistency between our high and low redshift galaxy samples. The masses assume the universal initial mass function (IMF) as parametrized by Kroupa (2001).

The aim of the first step of our work is to compare the SSFRs derived from the Balmer series with the SSFRs of Brinchmann et al. (2004, hereafter B04) derived from nebular emission lines. We begin with a subset of galaxies with $14.5 < r < 17.77$ and $0.005 < z < 0.22$ drawn from the DR4 spectroscopic sample. We divide galaxies with stellar masses in the range of $10^9 \sim 10^{12} M_{\odot}$ into 6 mass bins. The mass interval is set to $\Delta \log M_* = 0.5$. The SDSS spectra are obtained through a $3''$ circular fibre aperture, and therefore sample primarily the inner regions of galaxies. To minimize the effects of this so-called "aperture bias", we select galaxies with $0.9 < z/z_{\mathrm{max}} < 1$, where z_{max} is the highest redshift at which the galaxy in question would pass the sample selection criteria. In Table 1, we list the mass range and median redshift of galaxies in each mass bin.

2.2   The high redshift galaxy sample

In order to obtain accurate galaxy stellar masses at redshifts approaching unity, photometry in both optical and near-IR passbands is required. Our high redshift galaxy sample is selected from fields covered by both the DEEP2 galaxy redshift survey and the Palomar Observatory Wide Infrared Survey (POWIR).

Table 1. The mass ranges and median redshifts of galaxies in the 6 mass bins of the SDSS sample and 4 mass bins of the DEEP2 sample.

$\log M_*/M_\odot =$	$9.0 - 9.5$	$9.5 - 10.0$	$10.0 - 10.5$	$10.5 - 11.0$	$11.0 - 11.5$	$11.5 - 12.0$
z(SDSS)	0.05	0.07	0.09	0.14	0.17	0.20
z(DEEP2)	–	–	0.85	0.85	0.85	0.85

2.2.1 The DEEP2 Survey

The DEEP2 Galaxy Redshift Survey (Davis et al. 2003, Faber et al. in prep) utilizes the DEIMOS spectrograph (Faber et al. 2003) on the KECK II telescope. Targets for the spectroscopic sample were selected from BRI photometry taken with the 12k x 8k mosaic camera on the Canada-France-Hawaii Telescope (CFHT). The images have a limiting magnitude of $R_{AB} \sim 25.5$. As the R-band images have the highest signal-to-noise ratio (S/N) of all the CFHT bands, they were used to select the DEEP2 targets. The CFHT imaging covers four widely-separated regions, with a total area of 3.5 deg^2. In fields 2-4, the spectroscopic sample is preselected using $(B-R)$ and $(R-I)$ colors to eliminate objects with $z < 0.7$ (Davis et al. 2003). Color and apparent magnitude cuts were also applied to objects in the first field, the Extended Groth Strip (EGS), but these were designed to downweight low redshift galaxies rather than eliminate them entirely (Willmer et al. 2006). The third data release of the DEEP2 survey[1] contains spectra of about 50000 galaxies in the magnitude range $18.5 \leqslant R_{AB} \leqslant 24.1$. The spectra have a resolution of about $R \sim 5000$.

2.2.2 The Palomar Observatory Infrared Survey

K_s-band photometry was obtained in portions of all four fields targeted by the DEEP2 galaxy redshift survey using the Wide Field Infrared Camera (WIRC, Wilson et al. 2003) on the 5m Hale Telescope at the Palomar Observatory. Bundy et al. (2006) mapped the central third of fields 2-4 using contiguously spaced pointings tiled in a 3×5 pattern. About 85% of the pointings have a depth greater than $K_{AB} = 22$ and the imaging covers a total of 0.9 deg^2. In field 1 (the Extended Groth Strip), the K_s-band imaging covers 0.7 deg^2 to a typical depth of greater than $K_{AB} = 22.5$.

We use the stellar masses calculated by Bundy et al. (2006). They estimate the K_s-band mass-to-light ratios for the galaxies in this sample by comparing the optical to infrared spectral energy distributions (SEDs) to a grid of 13400 model SEDs generated using the BC03 code (Bruzual & Charlot 2003). The typical error in the stellar mass estimates is about 0.2dex. A Chabrier (2003) IMF is used: the systematic difference between the SDSS and DEEP2 stellar masses caused by the different choice of IMF is about 0.05dex. We correct for this by adding 0.05dex to the logarithm of the DEEP2 galaxy masses.

2.2.3 Our high redshift galaxy sample

The high redshift galaxy sample used in this work combines data from the DEEP2 and POWIR survey. The criteria used to select the galaxies are the following:

(i) The redshift range is $0.75 \leqslant z \leqslant 1$. This ensures that all the galaxy spectra fully cover the rest-frame wavelength range required to measure the spectral indices analyzed in this paper ($3750 - 4150$Å) (Note that the DEEP2 spectra span the wavelength range $6500 - 9100$Å).

(ii) The R-band magnitude range is $18.5 \leqslant R_{AB} \leqslant 24.1$. $R_{AB} = 24.1$ is the limit of the DEEP2 spectroscopic sample. By comparing with a fainter sample with photometric redshifts, Bundy et al. (2006) concluded that the spectroscopic sample is essentially complete down to $M_* \geqslant 10^{10} M_\odot$. As described in §4.1 we will correct for any residual incompleteness by applying a $1/V_{max}$ weight to each galaxy.

(iii) The K_s-band magnitude limit is $K_{AB} \leqslant 22$. The POWIR K_s-band survey covers different areas to different depths. $K_{AB} \leqslant 22$ is chosen to maximize the sky area covered, but also maintain a high level of completeness for galaxies with stellar masses $\log M_*/M_\odot \geqslant 10.0$. This K_s-band limit eliminates around 15% sources with $10 \leqslant \log M_*/M_\odot \leqslant 10.2$ from the $R_{AB} \leqslant 24.1$ sample. We show in §4.1 that this does not affect our results.

In summary, our DEEP2 sample has a redshift range $z \sim 0.75 - 1.0$, with $18.5 \leqslant R_{AB} \leqslant 24.1$ and $K_{AB} \leqslant 22$. It covers a total area of 1.6 deg^2 and the total source number is about 3000. The galaxies have a mean and median redshift of 0.87 and 0.85 respectively.

3 THE SPECTRAL INDICES

The 4000Å wavelength region of the galaxy spectrum contains abundant information for constraining the recent star formation histories of galaxies. Two traditionally-used indices, D4000 and Hδ_A, are located in this region. Importantly, this rest-frame wavelength region is usually included in both low and intermediate redshift galaxy surveys.

PCA is a standard multivariate analysis technique, designed to identify correlations in large datasets. Using PCA, Wild et al. (2007, hereafter W07) developed a set of new high signal-to-noise ratio spectral indicators located in the rest-frame wavelength range $3750 - 4150$Å. At wavelengths around 4000Å galaxy spectra vary in both spectral shape and strength of the Hydrogen Balmer absorption lines. These two are inversely correlated: younger galaxies have stronger Balmer absorption lines and weaker 4000Å break strengths. The third axis of variation is the CaII(H&K) lines, which are related to both the age and metallicity of the galaxy.

Because the DEEP2 spectra are not flux calibrated, the

---

[1] http://deep.berkeley.edu/DR3/

continua contain no useable information. In this work, we do not use the spectral indicators given by W07 but closely follow their method to create a similar set of indicators designed to work on high pass-filtered spectra. Because the continuum is removed by the filter process, we expect our eigenspectra to reveal the Balmer absorption lines as a primary axis of variation and CaII(H&K) lines as the secondary axis. We refer the reader to W07 for more details on the PCA method. Here we present the dataset and the methods used to obtain the indices and the resulting eigenspectra.

3.1   Input model data set for PCA

Our input data set for the creation of the PCA eigenspectra is a set of model spectra generated using the BC03 stellar population synthesis code (Bruzual & Charlot 2003). The model library is similar to that used in Kauffmann et al. (2003) and Salim et al. (2005), although with a more restricted parameter range. 6641 model galaxies are selected at random from the parent library according to the following criteria:

(i) The time t_{form} when the galaxy begins to form its stars is distributed uniformly between 0 and 5.7 Gyr after the Big Bang (the age of the universe is assumed to be 13.7 Gyr).

(ii) The model galaxies have exponentially declining star formation histories SFR $\propto \exp(-t/\tau)$ with τ distributed uniformally between $1 \leqslant \tau \leqslant 1.4$ Gyr.

(iii) Top-hat bursts are superimposed on these continuous models. Two parameters describe the bursts: f_{burst}, the fraction of the total stellar mass formed in bursts, is distributed logarithmically between 0.0 and 0.1; t_{burst}, the duration of the burst, is distributed uniformly between 0.03 and 0.3 Gyr. During the burst, stars form at constant rate. Bursts occur with equal probability at all times after t_{form} and the probability is set so that 50% of the galaxies in the library have experienced a burst over the past 2 Gyr.

(iv) The metallicity is distributed linearly in the range $0.5 \leqslant Z \leqslant 2Z_\odot$; no metallicity evolution is included.

These specific criteria (e.g. the distribution of t_{form}) are chosen so that the model galaxies span a reasonably wide and even range in mean stellar age. In this case, the Balmer absorption lines and CaII(H+K) absorption lines will be isolated in the output eigenspectra, and the Balmer absorption lines will dominate the first eigenspectrum and CaII(H+K) absorption lines the second eigenspectrum. We note that although changes to the input library will alter the resulting eigenspectra, our calibration using BC03 models in Section 5 ensures that we will recover the same SSFRs.

We convolve the model spectra to have a velocity dispersion equal to 150 km/s; this is the median value of the velocity dispersion of the galaxies in our samples. Each model spectrum is then normalised by the mean flux in the rest-frame wavelength range $4000 - 4080$Å, where the spectrum is free from strong absorption lines.

We smooth the spectrum F_λ with a Gaussian kernel $W(\lambda)$. This yields the low-pass spectral component

$$F_\lambda^{LP} = \frac{\int d\lambda' W(\lambda - \lambda') Ivar(\lambda') F_{\lambda'}}{\int d\lambda' W(\lambda - \lambda') Ivar(\lambda')} \qquad (1)$$
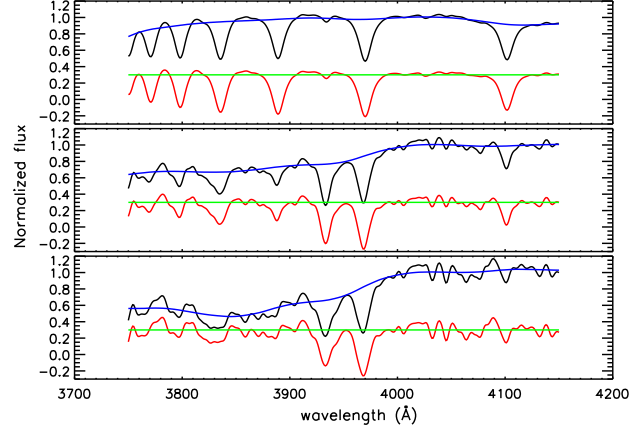
where

Figure 1. Examples of the filter process applied to the model spectra. Black: the original model spectrum. Blue: the low-pass filter component. Red: the resulting continuum filtered spectrum, shifted upwards for easy comparison with the original spectrum. Green: the zero point. Models have been selected to cover the full range of galaxy ages: galaxy age increases from top to bottom.

$$W(\lambda - \lambda') = \frac{1}{\sqrt{2\pi}\sigma} \exp\left[-\frac{1}{2} \left(\frac{\lambda - \lambda'}{\sigma} \right)^2 \right], \qquad (2)$$

and $\sigma = 32$Å. $Ivar(\lambda')$ is the inverse variance matrix of the spectrum. For the model spectrum, it is equal to 1 at all wavelength points. In the filtering process the strongest absorption lines are masked by setting $Ivar(\lambda') = 0$. We mask 20Å centred on $\lambda 4103, 3889, 3835$; 16Å centred on $\lambda 3798$; 12Å centred on $\lambda 3770, 3750$. The sizes of these masks were chosen to ensure that the absorption lines were not diluted in the filter process. Small changes to the mask sizes make no difference to the final results.

The high-pass component is then obtained as

$$F_\lambda^{HP} = F_\lambda - F_\lambda^{LP}. \qquad (3)$$

We choose to subtract the low-pass component, rather than divide by it as is commonly done, because we wish to retain the luminosity weighting of the real galaxies when they are stacked (see the following Section). Figure 1 shows three examples of the filtering process.

3.2   Creating the 'eigenspectra'

The model library is dominated by old galaxies. To ensure the dominance of the Balmer absorption lines in the first eigenspectrum, we weight each model spectrum by the reciprocal value of its 4000 Å break strength to reduce the impact of galaxies without strong Balmer absorption lines. The mean spectrum of the input data set is then calculated and subtracted, and the PCA is run to produce the eigenspectra.

Figure 2 presents the mean spectrum and first two eigenspectra of our input model galaxies. As required, the first eigenspectrum shows the Balmer series. The CaII(H&K) absorption lines are isolated in the second eigenspectrum. In the following section the first 10 eigenspectra are used to fit the SDSS and DEEP2 spectra. The coefficient of the first eigenspectrum ($PC1$, see eq.14), which
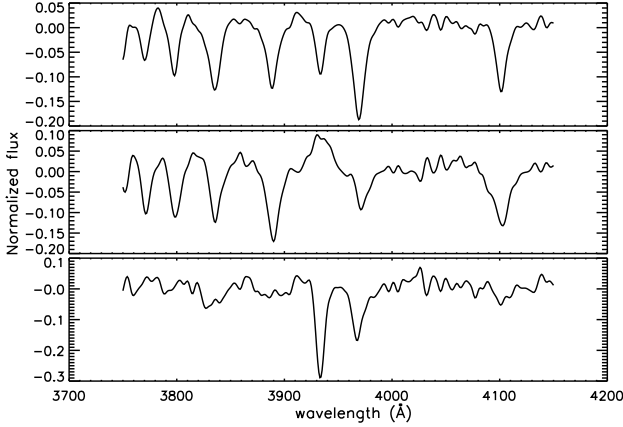
Figure 2. Top: the mean spectrum of the continuum filtered input data set. Middle: the first eigenspectrum in which the entire Balmer absorption line series is visible. Bottom: the second eigenspectrum, which shows the CaII(H&K) absorption lines.

represents the strength of Balmer absorption lines, is used to derive SSFRs.

4 DATA ANALYSIS

In this section, we describe how we apply our method to real data. Our methodology is similar to that of Glazebrook et al. (2003), who stacked a large number of SDSS spectra to create a "cosmic average" spectrum of all the stars in the Universe. The main difference is that we carry out the cosmic averaging in bins of stellar mass.

The steps of the analysis are the following:

• The galaxy spectra are corrected for foreground Galactic extinction and shifted to the restframe.

• The DEEP2 spectral resolution is about 3 times higher than that of the SDSS and the BC03 population synthesis models. In order to analyse SDSS and DEEP2 spectra in an equivalent manner, the DEEP2 spectra are convolved with a Gaussian kernel to match the resolution of the SDSS spectra.

• The spectra are rebinned to match the model wavelength binning.

• The spectra are converted into units of luminosity (see below for details).

• The continuum of the spectra is subtracted using the same filtering method used for the model spectra. An extra mask including 14Å centered on Ne III $\lambda 3783$ line is added.

All the filtered spectra in the same mass bin are stacked using the following weighting scheme:

$$L_{\rm comp}(\lambda) = \frac{\sum_{i=1}^{n} W(i) \times Ivar(i,\lambda) \times L(i,\lambda)}{\sum_{i=1}^{n} W(i) \times Ivar(i,\lambda)} \qquad (4)$$

where the sum is over $i = 1, 2, ..., n$ galaxies with individual luminosities $L(i,\lambda)$ in units of $\mathrm{erg\,s^{-1}\mathring{A}^{-1}}$. $Ivar(i,\lambda)$ is described below, and accounts for bad pixels and night sky lines[2]. $W(i)$ provides a weight for each source to correct for missing galaxies due to survey incompleteness.

_____

[2] For the DEEP2 spectra we make use of the code

For the flux calibrated SDSS spectra we convert to luminosity by scaling by the luminosity distance of the galaxies in the standard way. We set $Ivar(i,\lambda) = 0$ for bad pixels (identified in the SDSS mask array), otherwise $Ivar(i,\lambda) = 1$. The redshift intervals have been selected so that the samples are complete in mass and we therefore set $W(i) = 1$ for all galaxies.

For the DEEP2 galaxies, the spectra are not flux calibrated and cannot be converted directly into luminosity. In order to get $L(i,\lambda)$, we first normalise each individual spectrum over all wavelengths to its mean flux between $4000 - 4080$Å. This normalised spectrum is then scaled according to the optical photometry using the known spectroscopic redshift and optical colour information. The K-correction is derived from the best-fitting SED template output by the KCORRECT code (Blanton & Roweis 2007). The inverse variance matrix $Ivar$ includes only variations due to sky intensity, not object intensity[2]. This ensures that bad pixels are downweighted while equal weight is given to each spectrum.

Setting $Ivar(i,\lambda) = 1$ and down-weighting the noisy pixels give similar results for SDSS. But for DEEP2, these two methods give very different results. In order to get the same S/N of the composite spectra, we need to stack many more galaxies if we set $Ivar(i,\lambda) = 1$ than if we down-weight the pixels effected by sky lines in the DEEP2 spectra. This is because local galaxy spectra (SDSS) have much much higher S/N than high redshift galaxies (DEEP2) on average. The reason that individual pixel noise arrays are not used in the $Ivar$ array, is that this would overall downweight fainter galaxies, possibly introducing biases that are difficult to quantify into the composite spectra.

4.1 DEEP2 completeness correction

An issue with every data set is the selection of weights to correct for missing galaxies. The weights we use in this study take into account three factors:

• The target selection strategies of DEEP2.
• The redshift success rate.
• The magnitude limits.

The weight $W(i)$ for DEEP2 galaxy i is expressed as:

$$W(i) = \frac{\kappa_i}{V_{\max}^i} \qquad (5)$$

where κ_i accounts for incompleteness resulting from the DEEP2 color selection and redshift success rate. $V_{\max}^i$ accounts for the fact that faint galaxies are not detected throughout the entire survey volume in a magnitude-limited survey.

To calculate κ_i we closely follow the method described in Willmer et al. (2006), but add an extra dimension to the reference data cube, which is the K_s-band magnitude. For each galaxy in the photometric catalogue, we select all the galaxies from the redshift catalogue sharing the same bin in the $(B - R)/(R - I)/R_{\rm AB}/K_s$ space, count the number of objects with failed redshifts (N_f); the number of galaxies

COADD_SPECTRA.PRO available from the DEEP2 Team to identify bad pixels and separate sky from continuum noise.

with $z < z_l$ (N_{z_l}); the number of galaxies with $z > z_u$ (N_{z_u}); and the number of galaxies with successful redshifts within the "legal" redshift range z_l-z_u (N_z). For field 1 (the EGS), z_l=0.2, z_u=1.4; for fields 2-4, z_l=0.7, z_u=1.4. The probability that each galaxy in the photometric catalogue has a redshift in the legal range is estimated. For galaxies with high-quality redshifts, the probability $P(z_l \leqslant z \leqslant z_u)$=1 when $z_l \leqslant z \leqslant z_u$ and $P(z_l \leqslant z \leqslant z_u)$=0 if $z < z_l$ or $z > z_u$. The estimation of the probability for unobserved sources is based on the so-called "optimal" weighting model (see §2 of Willmer et al. 2006), which assumes that the failed redshifts of red galaxies have the same distribution as the successful ones, while blue galaxies with failed redshifts lie beyond the redshift limit z_u. Namely, for the red galaxies:

$$P(z_l \leqslant z \leqslant z_u) = \frac{N_z}{N_z + N_{z_l} + N_{z_u}} \tag{6}$$

for the blue galaxies

$$P(z_l \leqslant z \leqslant z_u) = \frac{N_z}{N_z + N_{z_l} + N_{z_u} + N_f} \tag{7}$$

Finally, κ_i is calculated by summing over all galaxies j in the photometric catalogue with the same $(B-R)/(R-I)/R_{AB}/K_s$ value as galaxy i, the probabilities that the redshifts of galaxies are within the legal limits

$$\kappa_i = \frac{\sum_j P(z_l \leqslant z \leqslant z_u)}{N_z} \tag{8}$$

In the case of EGS, a final correction is applied to κ_i to account for the different sampling strategy, which includes low-redshift ($z < 0.7$) galaxies but downweights them so that they do not dominate the sample. The correction factor (f_m) depends on the location of the galaxy in $(B-R)$ versus $(R-I)$ space and its apparent magnitude. f_m has been computed for around a quarter of the EGS galaxies from Willmer et al. (2006) for the purpose of measuring the galaxy luminosity function. We estimated f_m^i for the remaining galaxies in the EGS data to be the average f_m of all the galaxies within the same bin in the $(B-R)/(R-I)/R_{AB}$. The probability that a galaxy will be placed on an EGS mask is given by

$$P(\text{mask}) = 0.33 + 0.43 P_{\text{gal}} f_m \tag{9}$$

where P_{gal}, given in the DEEP2 catalogue, is the probability that an object is a galaxy based on its magnitude, color and size. For EGS galaxies,

$$\kappa_i = \frac{\sum_j P(z_l \leqslant z \leqslant z_u)}{N_z P(\text{mask})} \tag{10}$$

where j includes all the galaxies in the photometric catalogue which are within $(B-R)/(R-I)/R_{AB}/K_s$ space.

The calculation of $V_{\max}^i$ follows Schmidt (1968), and provides a simple way to account for the R-band limit of the sample. We define

$$V_{\max}^i = d\Omega \int_{z_{min,i}}^{z_{max,i}} \frac{dV}{dz} dz \tag{11}$$

where $d\Omega$ is the solid angle covered by the sample, $\frac{dV}{dz}$ is the comoving volume element and $z_{min,i}$ and $z_{max,i}$ are the low and high redshift limits within which galaxy i can be detected given the R-band limit of the survey. They are given by:
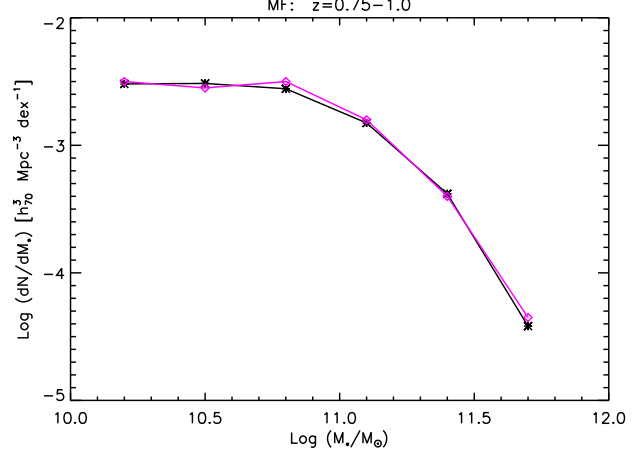

Figure 3. The stellar mass function for galaxies in the redshift range $0.75 - 1$. The black line is our result, the pink line is from Bundy et al. (2006).

$$z_{\max,i} = \min\{z'_{\max}, z(M_i, m_u)\}, \tag{12}$$

$$z_{\min,i} = \max\{z'_{\min}, z(M_i, m_l)\}, \tag{13}$$

where $z'_{\min}$ and $z'_{\max}$ are the redshift limits of the sample, $z(M_i, m_u)$ is the redshift above which the galaxy would be fainter than the R-band magnitude limit of 24.1 and $z(M_i, m_l)$ is the redshift below which the galaxy becomes brighter than $R_{AB} = m_l = 18.5$. We use the best-fitting SED templates output by KCORRECT to calculate $z(M_i, m_u)$ and $z(M_i, m_l)$. Because we are analyzing galaxies in a relatively narrow redshift slice, no evolutionary correction is applied.

In order to check that we recover the correct galaxy weights, we calculate the stellar mass function for the redshift bin $0.75 - 1$ and compare it to the result from Bundy et al. (2006). Figure 3 shows that the two stellar mass functions are almost identical.

In §2.2.3, we noted that some sources are missing in our $\log M_*/M_\odot = 10 - 10.5$ DEEP2 mass bin due to the additional $K_{AB} = 22$ magnitude limit. To test whether this incompleteness affects our final results, we repeat the entire analysis for a limiting magnitude $K_{AB} = 22.5$. This limit corresponds to a mass completeness limit of about $10^{10} M_\odot$. We find that our measured Balmer absorption line strengths in the lowest mass bin of DEEP2 remain the same to within the errors. If we were to increase the K_s-band magnitude limit to this fainter value for the whole sample, the area covered by the sample would decrease and this would affect our sample statistics, particularly for our highest mass bins.
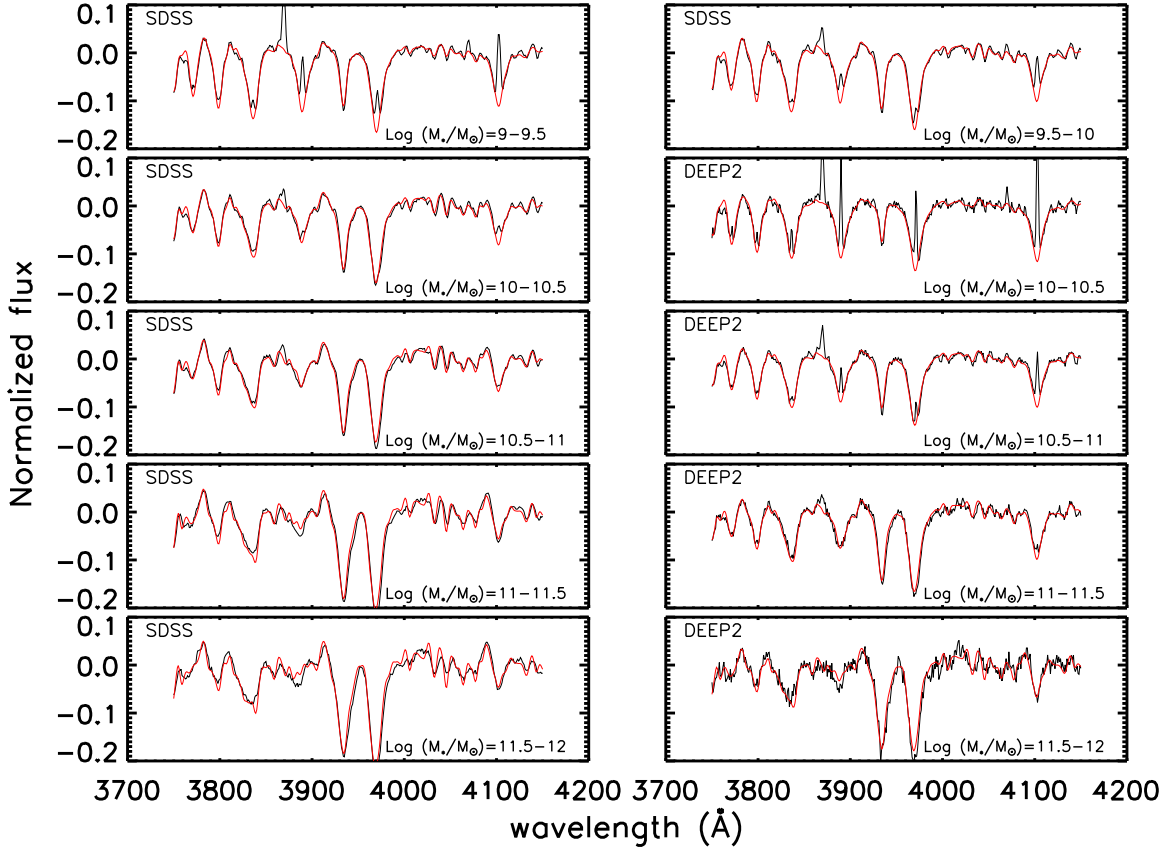
4.2   Fitting composite spectra

The PCA projection algorithm employed here accounts for pixel errors (Connolly & Szalay 1999) and allows the normalisation of the spectrum as a free parameter (G. Lemson, private communication, see W07). The fitting result is a linear combination of the eigenspectra,

$$L_{\text{comp}}(\lambda) = N \times \left(M + \sum_{i=1}^{10} PC_i \times E_i \right) \tag{14}$$

Table 2. Measured values of H_{balmer} and the SSFRs derived from them for each mass bin of SDSS and DEEP2. 'S' represents SDSS, 'D' represents DEEP2.

$\log M_*/M_\odot=$	$9.0 - 9.5$	$9.5 - 10.0$	$10.0 - 10.5$	$10.5 - 11.0$	$11.0 - 11.5$	$11.5 - 12.0$
$H_{\mathrm{balmer}}(\mathrm{S})$	0.04 ± 0.02	-0.08 ± 0.02	-0.20 ± 0.01	-0.34 ± 0.01	-0.46 ± 0.01	-0.53 ± 0.01
$\log \mathrm{SSFR}/\mathrm{yr}^{-1}(\mathrm{S})$	-9.80 ± 0.15	$-9.95^{+0.15}_{-0.10}$	$-10.35^{+0.15}_{-0.07}$	$-10.75^{+0.07}_{-0.15}$	$-11.15^{+0.07}_{-0.17}$	$-11.60^{+0.15}_{-0.55}$
$H_{\mathrm{balmer}}(\mathrm{D})$	$-$	$-$	0.03 ± 0.04	-0.11 ± 0.03	-0.21 ± 0.03	-0.46 ± 0.04
$\log \mathrm{SSFR}/\mathrm{yr}^{-1}(\mathrm{D})$	$-$	$-$	-9.40 ± 0.20	$-9.95^{+0.20}_{-0.15}$	-10.35 ± 0.15	$-11.30^{+0.20}_{-0.70}$

Figure 4. The composite spectra (black) and PCA fitted models (red, by eq.14) for all mass bins. The overall normalisation (N) has been divided out to make comparison easier.

where N is the normalization, M represents the mean spectrum (Figure 2, top). PC_i is the amplitude of the $i-$th eigenspectrum E_i, representing the amount of the $i-$th eigenspectrum present in the residual spectrum. These amplitudes are the new spectral indices which are calculated from the projection of each composite spectrum onto the eigenspectra. We note that principal component amplitudes can be negative, for example, negative $PC1$ means the strength of the Balmer absorption lines in the composite spectrum is weaker than that in the mean spectra. $E1$ represents the first eigenspectrum (Figure 2, middle), etc. In the current work, we are interested in the first index, which measures the strength of the Balmer series. We refer to it as 'H_{balmer}' from now on. We would like to stress that because we stack all spectra in each mass bin, the value of H_{balmer} relates to the "cosmic average" spectrum, which includes old galaxies with weak Balmer absorption lines.

Figure 4 shows the normalized composite spectra ($L_{\mathrm{comp}}(\lambda)/N$, black) and the the best-fit results (red). Both the strength of the Balmer absorption and the nebular emission lines in these spectra reveal that for the same mass bin, DEEP2 galaxies have much younger populations than SDSS on average. The values of H_{balmer} are listed in Table 2 for each mass bin of SDSS and DEEP2. Although statistical errors on the principal component amplitudes are calculated during the projection of the eigenspectra, they are insignificant with respect to the errors caused by the sample size. We estimate the sample variance errors using a bootstrap technique, by sampling with replacement the same number of galaxies as are in the stack, and recalculating H_{balmer} 100

times. The errors are given by the root-mean-square difference between the H_{balmer} values calculated for each bootstrap sample and the mean value.

5   ESTIMATING SPECIFIC SFR

When stacking many hundreds of galaxy spectra, it is reasonable to assume that stochastic fluctuations in the star formation histories of individual galaxies will average out, and that the star formation history of the composite "galaxy" can be approximated by a smooth function. In this section, we work with a grid of exponentially declining star formation models constructed from the BC03 population synthesis code. We create 10^6 different models by varying the following parameters:

(1) The formation time of a galaxy (t_{form}) is defined as the time since the Big Bang when the galaxy first begins to form its stars and is uniformly distributed between 0 and 10 Gyr.

(2) The star formation rate is modelled as SFR $\propto$ $\exp(-t/\tau)$, with an e-folding timescale τ uniformly distributed in the range $0.01 - 10$ Gyr.

(3) We calculate three sets of models with metallicities $Z = 0.02 = Z_{\odot}$, $Z = 0.008$ and $Z = 0.004$. According to the mass-metallicity relation (Gallazzi et al. 2005; Panter et al. 2008), the average global metallicity is near solar for the galaxies with stellar masses greater than $10^{10} M_{\odot}$. For galaxies with stellar masses smaller than $10^{10} M_{\odot}$, most galaxies have sub-solar metallicity, but the metallicity increases rapidly with stellar mass. In the following, we will assume the observed mass-metallicity relation and use solar metallicity models for mass bins with $M_* \geqslant 10^{10} M_{\odot}$, models with $Z = 0.008$ for the mass bin with $9.5 \leqslant \log M_*/M_{\odot} \leqslant 10$, and $Z = 0.004$ models for the mass bin with $9 \leqslant \log M_*/M_{\odot} \leqslant 9.5$.

(4) We consider models with and without dust. The effects of dust attenuation on the spectral properties are computed according to the simple two-component model of Charlot & Fall (2000). The total effective V-band optical depth τ_V of the models is set to be a Gaussian distribution with peak at 1.6 and standard deviation of about 0.8. If $\tau_V < 0$, we set it to zero. This distribution is similar to the SDSS DR4 star forming galaxies with stellar masses in the range of $10^9 - 10^{12} M_{\odot}$. The parameter μ, the fraction of the dust optical depth contributed by the 'ambient' interstellar medium, is set to be 0.3. We will show later that our results are not greatly affected by dust.

We extract the spectrum for each of our model galaxies at an age $age_{\mathrm{model}} = t_{\mathrm{H}}(z) - t_{\mathrm{form}}$, where $t_{\mathrm{H}}(z)$ is the age of universe at redshift z, and z corresponds to the median redshifts of our SDSS and DEEP2 samples. They are listed in Table 1. After broadening the spectra to a velocity dispersion of 150km/s and filtering out the continua, we measure the values of H_{balmer} for each of the model spectra. The parameters of the models that best fit the H_{balmer} values measured for the composite spectra, are obtained by weighting each model in the library by the probability function $\exp(-\chi^2/2)$, and then binning the probabilities as a function of the given parameter value (see Appendix A of Kauffmann et al. 2003 for a detailed description). The most probable value of a model parameter for a particular com-
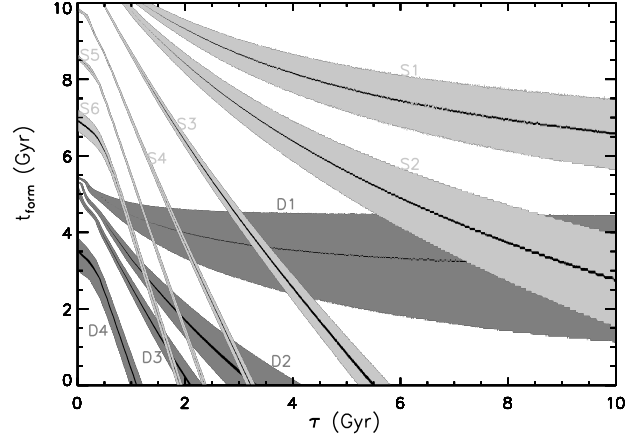

Figure 5. Probability contours of t_{form} versus τ for galaxies in different stellar mass bins. They represent the 68% confidence regions. Results are shown for SDSS (light grey areas) and for and DEEP2 (grey areas). The labels 'S' and 'D' in this plot represent SDSS and DEEP2, respectively. 'S1' means the first mass bin of SDSS, with $\log M_*/M_{\odot} = 9.0 - 9.5$; 'S2' with $\log M_*/M_{\odot} = 9.5 - 10.0$; 'S3' with $\log M_*/M_{\odot} = 10.0 - 10.5$; 'S4' with $\log M_*/M_{\odot} = 10.5 - 11.0$; 'S5' with $\log M_*/M_{\odot} = 11.0 - 11.5$; 'S6' with $\log M_*/M_{\odot} = 11.5 - 12.0$; 'D1' with $\log M_*/M_{\odot} = 10.0 - 10.5$; 'D2' with $\log M_*/M_{\odot} = 10.5 - 11.0$; 'D3' with $\log M_*/M_{\odot} = 11.0 - 11.5$; 'D4' with $\log M_*/M_{\odot} = 11.5 - 12.0$.

posite spectrum can be taken as the peak of this distribution; the most typical value is its median. In the following sections, we use the median of the probability distribution as our adopted best estimate.

Figure 5 shows our best-fit results in the space of τ versus t_{form}. The shaded areas denote 68% confidence regions with $|H_{\mathrm{balmer}}(m) - H_{\mathrm{balmer}}(d)| \leqslant 1\sigma$, where $H_{\mathrm{balmer}}(m)$ is the value of H_{balmer} measured from the model galaxy spectrum. $H_{\mathrm{balmer}}(d)$ is measured from the composite spectrum, σ is its error. Light grey regions correspond to the 6 stellar mass bins for the SDSS sample, while dark grey regions correspond to the 4 DEEP2 mass bins. The central black lines show the best-fit results. As shown in Figure 5, there is a strong degeneracy between τ and t_{form}, so the 1-σ contours appear as strips, rather than compact regions in the plot. However, it is clear that the mass bins separate clearly in τ-t_{form} space, indicating different mass galaxies have had significantly different *recent star formation histories.*

Rather than using our model grid to estimate the parameters t_{form} and τ, which we have shown are degenerate, we now turn to a parameter that directly characterizes the recent star formation histories of the galaxies that make up our composite spectra. We remind the reader that the Balmer absorption lines are most sensitive to stars that have formed over the past $10^8 - 10^9$ years. In the spectra of individual galaxies, the Balmer absorption lines have often been used as a *post-starburst* indicator, because they remain strong for nearly a Gyr after the burst has already ended. For our composite spectra, however, bursts are not of relevance and our approach in this paper will be to use H_{balmer} as a measure of the average specific star formation rate (SSFR= $\langle \mathrm{SFR} \rangle / \langle \mathrm{M}_* \rangle$) of the galaxies in the stack.

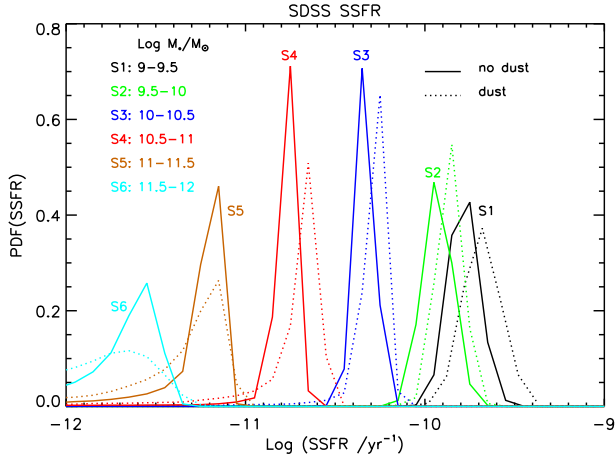We use the Balmer absorption lines as our SSFR indi-

Figure 6. The probability distributions of the SSFRs for SDSS galaxies. Lines with different colors represent different mass bins. The SSFRs decrease with increasing mass. Solid lines show SSFRs estimated using BC03 models without dust, while dashed-lines show the results using models with dust.
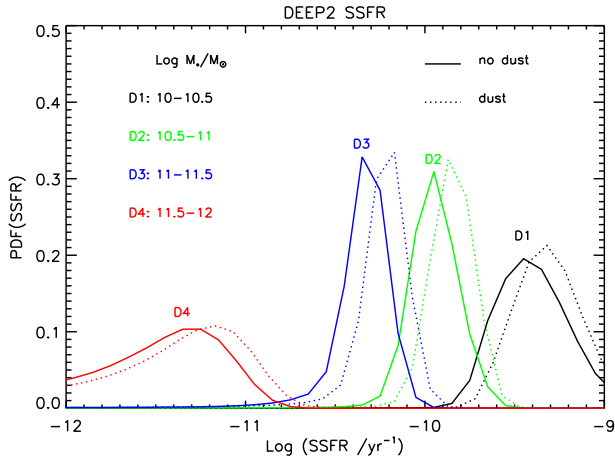

Figure 7. Same as Figure 6, but for DEEP2.

cator. These are mainly contributed by A stars (see Figure 1 of W07), which have a lifetime of several hundred million years. So long as the star formation rates of our composite galaxies are evolving on timescales that are significantly longer than this, our estimate should agree with those that use shorter-timescale indicators such as emission lines or IR photometry. In the next subsection, we will test this assertion using a catalogue of galaxy spectra generated using a cosmological simulation.

In Figures 6 and 7, we show the probability distributions of the parameter SSFR for each mass bin of the SDSS and DEEP2 galaxy samples. The solid lines show SSFRs estimated using BC03 models without dust, while dashed-lines show the results from models with dust. As can be seen, the results agree with each other to within 0.15dex, because dust has a very weak effect on the Balmer absorption line series. From now on, we will quote results based on models without dust.

In Figure 8, we plot the median values of the probability distribution functions (PDF) of SSFR as a function
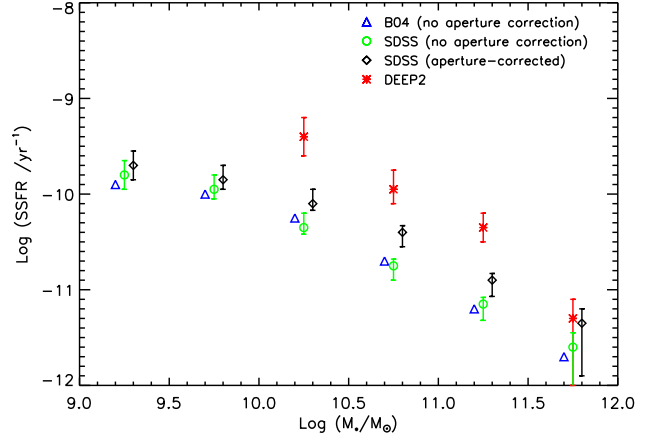

Figure 8. SSFRs as a function of stellar mass. Green circles show the SDSS results. Blue triangles show the fibre SSFRs estimated by B04. Black diamonds show aperture-corrected SDSS SSFRs. The blue triangles and black diamonds have been slightly displaced in the x-axis (by minus and plus 0.05dex, respectively) to allow the error bars to be distinguished. Red asterisks: SSFRs for the four DEEP2 mass bins.

of stellar mass for the galaxies in the SDSS (green circles) and DEEP2 (red asterisks) samples. The error bars on each point indicate the 68 percentile range in the PDF around the median. As can be seen the widths of the PDFs are quite narrow, indicating that the formal error on our estimates of SSFR are small.

5.1 Aperture effects

When we compare the low redshift and high redshift measurements we must account for aperture effects.

The SDSS spectra are obtained through $3''$ diameter fibres. At the median redshift of our sample, only the central 25% of the galaxy light has been included, so aperture effects will affect the SSFR estimates, particularly for early-type spiral galaxies where the light from the central few kpc will be dominated by the bulge component of the galaxy and light from the disk will be underrepresented. The DEEP2 spectra are taken through $1''$ slits; the typical galaxy in our high-z sample has a diameter of $\leqslant 2''$. Aperture effects will thus be less of an issue here, unless SFR gradients are significantly stronger at high z, which seems unlikely (Dominguez-Palmero & Balcells 2008).

When we compare the SDSS and DEEP2 SSFR measurements in subsequent sections, we must use aperture-corrected values for the SDSS galaxies. We do this by applying the corrections estimated by B04. They use the $g - r$ and $r - i$ colors measured outside the fibre to estimate the amount of star formation in the outer parts of the galaxies. We note that Salim et al. (2007) showed that this correction is an overestimate for certain classes of galaxies, such as AGN and galaxies without detectable Hα emission. Comparing the average aperture-corrected SSFR of B04 in each mass bin with the results from Salim et al., we find that except for the most massive bin ($\log M_*/M_\odot = 11.5 - 12$), the discrepancy is negligible. We have thus decided to apply the B04 correction to our 6 SDSS mass bins and the

results are shown in Figure 8 as black diamonds (they have been displaced in the x-axis by plus 0.05dex to allow the error bars to be distinguished). The aperture correction increases the value of SSFR by ~ 0.15dex at $M_* \leqslant 10^{10} M_\odot$ and $0.2 \sim 0.3$dex at $M_* > 10^{10} M_\odot$ We have not applied any similar correction to the high-z data. We will discuss this issue in more detail in §6.2.

Comparing our results for SDSS and DEEP2 presented in Figure 8 leads to two main conclusions:

(i) At stellar masses above $10^{10} M_\odot$, in both the low redshift and the high redshift samples, the SSFRs decrease monotonically and relatively steeply with stellar mass (SSFR $\propto M_*^{-(0.85 \sim 0.9)}$) .

(ii) The average SSFR decreases by a factor of $\sim 3 - 4$ from $z \sim 1$ to $z \sim 0$, and this factor appears to be independent of galaxy mass.

5.2   Tests of the method

We have claimed that our method of estimating the average SSFR of a stacked sample of galaxies using $H_{\rm balmer}$ should agree with other, more traditional methods that make use of indicators that are sensitive to star formation over much shorter timescales.

In this section, we test this claim in two different ways. Our first test is a *direct* one. B04 have estimated SSFRs for the SDSS galaxies in our sample using emission line fluxes (the greatest weight is carried by Hα). For AGN and galaxies without detectable Hα emission, the SSFR is estimated from the 4000 Å break strength measured within the fibre, using the relation between D4000 and SSFR calibrated using star forming galaxies.

The blue triangles in Figure 8 show the average SSFRs from B04 for exactly the same sample of galaxies used to derive the green circles. We shift the blue triangles in the x-axis direction by minus 0.05dex to make the comparison clear. We find very good consistency between the two methods, suggesting that $H_{\rm balmer}$ does provide a good measure of the average SSFR of a population of galaxies and that our methodology is robust. We note that the SSFRs derived by B04 from nebular emission lines agree well with those derived from multi-wavelength SED fitting including UV fluxes by Salim et al. (2007). This provides yet another confirmation of the robustness of the method.

We cannot test our estimates of SSFR for the DEEP2 galaxies in the same way, because Hα has shifted out of the relevant spectral range. Instead, we test our method using a DEEP2 mock catalogue of galaxy spectra that has been generated from the Millennium Run simulation (Springel 2005). We first construct a 2×2 sq. deg. mock catalogue using the MoMaF software (Blaizot et al. 2005) and the semi-analytic prescription for galaxies from De Lucia & Blaizot (2007) [3]. An important ingredient of this model, inherited from the work of Croton et al. (2006), is the AGN feedback implementation, which prevents cooling flows in massive haloes, and hence quickly shuts down star formation in massive galaxies. In lower mass haloes, where cooling continues unhampered by AGNs, the rate at which new cold gas
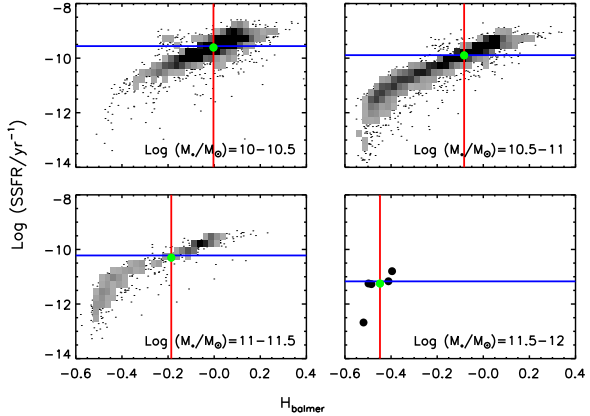
---

[3] The data for this model are publically available at http://www.mpa-garching.mpg.de/millennium

---

Figure 9. SSFRs as a function of $H_{\rm balmer}$ for model galaxies in the DEEP2 mock catalogue with redshifts in the range $0.75 \leqslant z \leqslant 1$. Blue lines mark the mean SSFRs of galaxies in the mock catalogue evaluated directly from the stellar masses and SFRs predicted by the semi-analytic model. Red lines mark the values of $H_{\rm balmer}$ measured from the composite spectra. The green dots show the SSFRs derived from $H_{\rm balmer}$. The last panel has so few objects that they are shown as black points rather than greyscale.

---

reaches the galaxy and the efficiency of galactic winds regulate the rate at which stars form. We select mock galaxies to match the DEEP2/POWIR magnitude selection, namely with $18.5 \leqslant R_{\rm AB} \leqslant 24.1$ and $K_{\rm AB} \leqslant 22$. We compute the stellar SED of each selected mock galaxy using its complex star formation history and metallicity evolution predicted by the semi-analytic model (SAM), combined with the BC03 stellar population library. In the end, for each mock galaxy, we thus have an "observed" SED plus a set of properties (z, M_*, SFR) taken directly from the output of the SAM. Although this catalogue may not be a perfect representation of the real Universe, the co-moving star formation rate density does increase at higher redshifts at a rate similar to that observed (see Kitzbichler & White 2007 for a discussion). The catalogue should thus provide a good way to test our methodology using a sample of galaxies that is forming stars more actively than those in the local Universe.

As seen in Figure 1 of W07, the strength of Balmer absorption lines decreases not only for old stellar populations, but also for the very youngest stellar populations, which are dominated by O stars with weak absorption lines. If very young galaxies dominate the high redshift samples, then one might worry that the method might underestimate the specific star formation rates, simply because an O-star dominated stellar population would be mistaken for a much older one. We use the DEEP2 mock catalogue to show that at redshifts ~ 1, the average galaxy is not sufficiently young that this becomes a serious concern.

We have selected galaxies with $0.75 \leqslant z \leqslant 1$ from the DEEP2 mock catalogue and divided them into mass bins in exactly the same way as was done for the real data. The analysis of the model galaxies (including the stacking and filtering procedure) is also carried out in the same way as for the real data. In Figure 9, we plot SSFR as a function of $H_{\rm balmer}$ for each individual model galaxy. Results are shown for four different mass bins. The blue lines show the average

SSFR of all the galaxies in the bin, defined as $\langle \text{SFR} \rangle / \langle \text{M}_* \rangle$. Red lines are the values of H_{balmer} measured from the composite spectra. The green dots show the SSFRs derived from H_{balmer} of composite spectra. As can be seen, the values obtained from the stacks are almost exactly the same as those obtained from the average instantaneous SSFR calculated from the model galaxies.

6   DISCUSSION

In this section, we translate SSFR into a dimensionless star formation activity parameter (see Davé 2008), defined as

$$\alpha_{sf} \equiv \frac{1}{\text{SSFR}} \frac{1}{t_{\text{H}}(z) - 1\text{Gyr}}. \tag{15}$$

Physically, this can roughly represent the fraction of the Hubble time (minus a Gyr) that a galaxy needs to have formed its stars at its current rate in order to produce its current stellar mass[4]. A Gyr is subtracted in order to take account of the fact that dark matter halos massive enough to host galaxies with reasonably high star formation rates take about 1 Gyr to assemble in a ΛCDM Universe (Davé 2008). A value of α_{sf} of 1 indicates that the galaxies could feasibly have formed all their stellar mass by forming stars continuously at the rate now observed. If α_{sf} is greater than 1, their past average SFR must have been greater than their current SFR for the stellar mass of the galaxy to have formed within a Hubble time.

In Figure 10, we show our estimate of this characteristic timescale α_{sf} as a function of stellar mass at both high (red asterisks) and low (black diamonds) redshifts. We remind the reader that the low-z, highest mass bin is uncertain due to aperture correction complications in the SDSS survey. From this plot, we find that α_{sf} is a strongly increasing function of M_*; the timescale increases from values close to a Hubble time for galaxies with $10^{10} M_\odot$ to more than an order of magnitude larger than the Hubble time for galaxies more massive than $10^{11} M_\odot$. We find that, at fixed stellar mass, $\log \alpha_{sf}$ evolves only slightly with redshift, decreasing by around 0.2dex between $z \sim 0$ and $z \sim 1$.

6.1   Comparison with galaxy formation models

The blue squares in Figure 10 (displaced in the x-axis by plus 0.05dex to make the comparison clear) show the characteristic timescale of star formation in the mock DEEP2 universe created from the Millennium run SAM as described in Section 5.2. A key result of this paper is that the model is entirely consistent with observational results at $z \sim 1$, both in amplitude and slope.

More generally, in theoretical models of galaxy formation, at a fixed stellar mass, α_{sf} is predicted to remain constant out to redshifts greater than 2 (Figure 2 of Davé 2008). This latter result is robust to methodology, both semi-analytic and smooth-particle-hydrodynamic (SPH) simulations agree. Specifically, between a redshift of 1 and 0 the models predict changes in $\log \alpha_{sf}$ of less than 0.1dex. Our

[4] We note that α_{sf} is not simply the fractional Hubble time the galaxy takes to form its stars, because stellar mass is returned to the ISM, a fact which is not accounted for in this simple model.
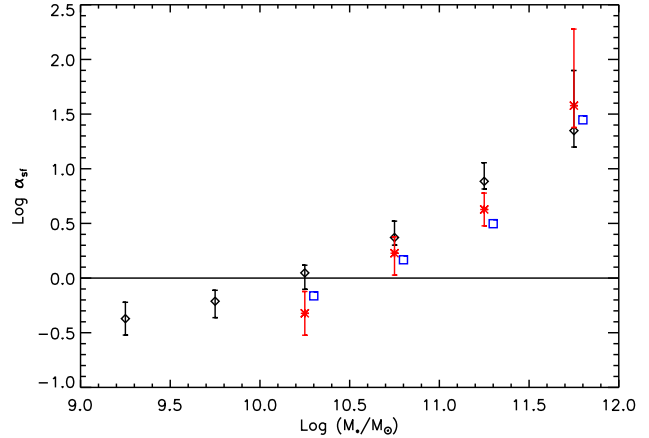
Figure 10. Star formation activity parameter α_{sf} as a function of stellar mass. As in previous plots, black diamonds and red asterisks represent SDSS and DEEP2 results, respectively. Blue squares are the results derived from the DEEP2 mock catalogue, they have been displaced in the x-axis by plus 0.05dex to make the comparison clear.

observational results indicate a slightly larger increase of 0.2dex. Further studies using larger surveys will be required to confirm this small amount of evolution.

The amplitude of α_{sf} and its variation with stellar mass depend on simulation methodology. The near unity α_{sf} at both $z \sim 0$ and $z \sim 1$ for galaxies with $M_* \lesssim 10^{10.5} M_\odot$ suggests that galaxy mass growth in this mass and redshift range may be dominated by smooth and steady cold mode accretion, as implemented in all current models of galaxy formation. The strong increase of α_{sf} with M_* that we observe at both redshift 1 and in the local Universe (Figure 10), is an expression of the phenomenon of 'downsizing': massive galaxies have apparently completed most of their star formation at higher redshifts than low mass systems. In many current models of galaxy formation, the explanation of this behaviour is "AGN feedback". More massive galaxies are more likely to host massive black holes which have the capability of producing more energy. Of equal importance, these massive galaxies are hosted by larger halos, where the AGN energy can be well coupled to the material that would otherwise cool and fuel star formation in the galaxies. As a result, AGN feedback through heating of the interstellar and intergalactic gas is more efficient in massive galaxies.

In summary, the observed amplitude and evolution of α_{sf} as presented in this paper, provide firm constraints for all galaxy formation models.

6.2   Comparison with previous results

As we have shown, our results appear to be in good general agreement with cosmological galaxy formation models. We now turn to a comparison with previous results from the literature. As we shall show, there is a significant discrepancy of $0.3 - 0.4$dex between our H_{Balmer} derived SSFRs, and those derived primarily from multiwavelength broad band photometry.

The results from two other studies of the SSFRs of galaxies at $z \sim 1$ are compared with our results in Fig-
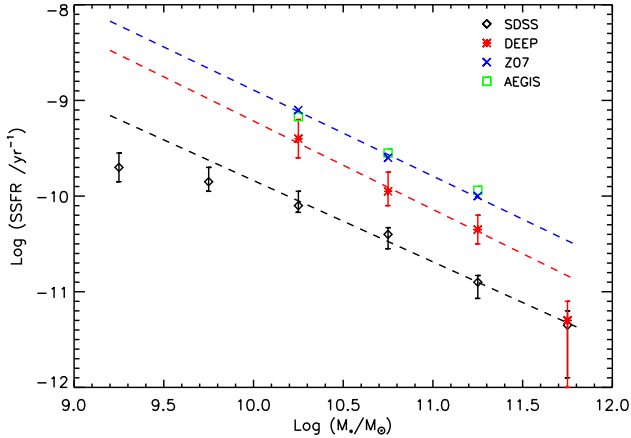
Figure 11. SSFR as a function of stellar mass. Black diamonds: aperture-corrected SDSS data. Red asterisks: SSFRs of DEEP2 galaxies. Blue crosses and green squares: SSFRs from Z07 & AEGIS respectively.

ure 11. The blue crosses represent SSFRs derived from the COMBO-17 sample with Spitzer $24\mu m$ and GALEX data (Zheng et al. 2007, hereafter Z07). These authors use the measured UV+IR luminosities to derive SFRs (Bell et al. 2005). They take account of the contribution from galaxies that are not individually detected at $24\mu m$ by stacking their images.

The green squares show results calculated by us for a sample of galaxies selected from the All-Wavelength Extended Groth Strip International Survey (AEGIS). The galaxies are a subsample of those used to create the composite spectra in this paper. This sample is not exactly the same as presented in Noeske et al. (2007, hereafter N07) and Noeske et al. (2007b), as only star-forming galaxies were included in their analysis. Instead, we have averaged the SSFRs over all the galaxies in each stellar mass bin (i.e. both star-forming and quiescent ones), using the same weighting factors that we used in our spectral stacking analysis. Aside from this difference in sample, the method used to derive SFRs for the AEGIS galaxies is the same as used by N07.

The method used by N07 to derive SFRs is slightly different to that employed by Z07, in that information from emission lines in the spectra of the galaxies is utilized if it is available. For galaxies with $f_{24\mu m} > 60\mu Jy$ and strong emission lines, the total SFR is derived from a combination of the IR measurements and from DEEP2 emission lines (Hα, Hβ, or [O II]$\lambda3727$, depending on z) with no extinction correction. SFRs are derived from extinction-corrected emission lines only for blue galaxies with strong emission lines and no detectable 24 micron emission. Red galaxies with weak emission lines, but no 24 micron detections, are considered star-forming and SFRs are derived from emission lines, assuming the same extinction corrections as for normal star-forming galaxies.

The dashed lines in Figure 11 are a linear fit to the data points for mass bins with $\log M_*/M_\odot \geqslant 10$. As can be seen from this plot, the slope of the relation between SSFR and mass that we derive is consistent with the results of AEGIS and Z07. However our method yields a normalisation that is $0.3 - 0.4$dex lower than AEGIS and Z07.

This discrepancy is puzzling, but it does have a number of possible explanations:

1) *Systematic differences in the calibration of different SFR indicators.* Our method is based on stellar absorption line indicators, while the N07 and Z07 results are based on a combination of UV, IR and emission lines. We have demonstrated that our results do agree with the SSFRs derived by B04 from emission lines at low redshift, which provides confidence that there is no significant discrepancy between our method and the standard calibration of extinction-corrected Hα to derive SFR. We are unable to carry out the same test at $z \sim 1$, because Hα is redshifted out of the spectral range covered by most galaxy surveys. Systematic differences in estimated stellar mass do occur when different population synthesis models are used due to differing mass-to-light ratios in the models. However, the same BC03 models have been used in the comparison to the AEGIS results.

2) *Obscured AGN.* There has been no attempt to remove obscured AGN from the two $z = 1$ galaxy samples with which we compare. Both the N07 and Z07 analyses make use of the 24 micron Spitzer passband as a star formation indicator. At $z = 1$, this corresponds to a rest-frame wavelength of 12 micron, which is very close in wavelength to where emission from a dusty torus would become very significant (see e.g. Daddi et al. 2007). In addition, AGN emission could well be contaminating some of the optical emission lines used to estimate SFR. By contrast, the H_{balmer} index originates from stellar atmospheres and is not expected to be contaminated from emission from an obscured AGN.

On the other hand, the vast majority of DEEP2 24 micron sources and line–emitting galaxies have line ratios indicating star formation and not AGN (Weiner et al. 2007). If the AGN were highly obscured, they could contribute at 24 micron and not show up in optical lines, but to make up a difference of 0.3dex one would have to assign half of the $24\mu m$ emission at z=1 to obscured AGN, which would appear quite extreme (B. Weiner, private communication).

3) *Evolution of IMF with redshift.* The SFR indicators used by N07 and Z07 trace O and B stars, whereas our SFR indicator is the Balmer series and is mainly influenced by A stars. If the IMF changes with redshift such that more massive stars form at higher z (e.g. Davé 2008; van Dokkum 2008), then a discrepancy between the two methods may not be apparent in the analysis of the low redshift samples, but may become more pronounced at higher z.

4) *Aperture effects.* As we have discussed, the SSFRs we estimate for the $z = 1$ galaxies may be biased somewhat low because the long-slit spectra preferentially sample the inner bulge of the galaxy. However, 95% of the DEEP2 galaxies (at all redshifts) with a line measurement have $r_{eff} < 0.95''$ as measured in the CFHT imaging (Weiner et al. 2007). Thus the $1''$ slit covers a large fraction of the galaxy. Additionally the seeing mixes the light into the slit to a much greater degree in DEEP2 than it does for the SDSS fibers. Thus the star formation gradients of $z = 1$ galaxies would have to be extremely strong for this to make a factor $2 - 3$ difference to the SSFR estimated for the galaxy population as a whole. As can be seen from Figure 8, the correction for aperture effects in the low z sample is only a factor of 2 on average, even in the case where the fibre only samples 25% of the total light.

In this paper, we are not able make a definitive con-

clusion with regard to the possibilities listed above. It is clear that there are many inherent uncertainties in estimating SFRs in galaxies and that more work is needed before the factors of $2 - 3$ offsets that we see between the different methods and the models can be understood in detail.

7 SUMMARY

In this paper, we developed a new method to measure the average SSFR of a population of galaxies using the Balmer absorption line series located in the rest-frame wavelength range $3750 - 4150$Å. Our method is free of complications due to dust extinction and AGN contamination, and provides a consistent way to measure SSFRs at both high and low redshifts. The robustness of the method has been tested using SDSS data and a DEEP2 mock catalogue drawn from cosmological simulations.

We apply this method to the DEEP2 galaxy sample. We high-pass filter the spectra because the DEEP2 spectra are not flux calibrated and then stack together the spectra of galaxies with similar stellar masses. SSFRs are estimated from the Balmer absorption line series by comparing to a library of model spectra generated from the BC03 stellar population code.

Our results show that:

• The average SSFR decreases monotonically with stellar mass at both $z \sim 0$ and $z \sim 1$. At both redshifts the decrease is almost an order of magnitude between $10^{10} M_\odot$ and $10^{11.5} M_\odot$.

• For galaxies of fixed stellar mass, the average SSFR has decreased by a factor of $3 - 4$ from $z \sim 1$ to $z \sim 0$.

• The amplitude of the decrease in SSFR with z is independent of stellar mass in the stellar mass range observable in the high redshift sample, i.e. $10^{10} - 10^{11.5} M_\odot$.

• The average SSFR of galaxies at $z \sim 1$ is consistent with the predictions of the semi-analytic model of De Lucia & Blaizot (2007) in all stellar mass bins observed.

We define a star formation activity parameter α_{sf} which is the average time (in units of the Hubble time at redshift z) needed by a galaxy of a given mass to form its stars at its current SFR. We find that galaxies of mass $\lesssim 10^{10.5} M_\odot$ are consistent with $\alpha_{sf} \sim 1$. This is in good agreement with models in which star formation is regulated by the infall of cold gas. At higher masses α_{sf} increases sharply, which, in the currently favoured galaxy formation scenario, can be understood by AGN feedback reducing the rate at which gas cools onto more massive galaxies.

REFERENCES

Adelman-McCarthy J. K., Agüeros M. A., Allam S. S. et. al (The SDSS Collaboration), 2006, ApJS, 162, 38

Bauer A. E., Drory N., Hill G. J., Feulner G., 2005, ApJ, 621, L89

Bell E. F., Papovich C., Wolf C. et al., 2005, ApJ, 625, 23

Benson A. J., Bower R. G., Frenk C. S., Lacey C. G., Baugh C. M., Cole S., 2003, ApJ, 599, 38

Blaizot J., Wadadekar Y., Guiderdoni B., Colombi S. T., Bertin E., Bouchet F. R., Devriendt J. E. G., Hatton S., 2005, MNRAS, 360, 159

Blanton M. R., Roweis S., 2007, AJ, 133, 734

Bower R. G., Benson A. J., Malbon R., Helly J. C., Frenk C. S., Baugh C. M., Cole S., Lacey C. G., 2006, MNRAS, 370, 645

Brinchmann J., Charlot S., White S. D. M., Tremonti C., Kauffmann G., Heckman T., Brinkmann J., 2004, MNRAS, 351, 1151

Bruzual G., Charlot S., 2003, MNRAS, 344, 1000

Bundy K., Ellis R. S., Conselice C. J. et al., 2006, ApJ, 651, 120

Chabrier G., 2003, PASP, 115, 763

Charlot S., Fall S. M., 2000, ApJ, 539, 718

Cole S., Lacey C. G., Baugh C. M., Frenk C. S., 2000, MNRAS, 319, 168

Connolly A. J., Szalay A. S., 1999, AJ, 117, 2052

Croton D. J., Springel V., White S. D. M. et al., 2006, MNRAS, 365, 11

Daddi E., Alexander D. M., Dickinson M. et al., 2007, ApJ, 670, 173

Davé R., 2008, MNRAS, 385, 147

Davis M. et al., 2003, Proc. SPIE, 4834, 161

Dekel A., Birnboim Y., 2008, MNRAS, 383, 119

De Lucia G., Blaizot J., 2007, MNRAS, 375, 2

De Lucia G., Springel V., White S. D. M., Croton D., Kauffmann G., 2006, MNRAS, 366, 499

Dominguez-Palmero L., Balcells M., 2008, ArXiv e-prints, 0807.3053

Faber S. M. et al., 2003, Proc. SPIE, 4841, 1657

Feulner G., Gabasch A., Salvato M., Drory N., Hopp U., Bender R., 2005, ApJ, 633, L9

Gallazzi A., Charlot S., Brinchmann J., White S. D. M., Tremonti C. A., 2005, MNRAS, 362, 41

Glazebrook K., Baldry I. K., Blanton M. R. et al., 2003, ApJ, 587, 55

Guo Q., White S. D. M., 2008, MNRAS, 384, 2

Heavens A., Panter B., Jimenez R., Dunlop J., 2004, Nature, 428, 625

Hopkins P. F., Hernquist L., Cox T. J., Robertson B., Springel V., 2006, ApJS, 163, 50

Kauffmann G., Heckman T. M., White S. D. M., 2003, MNRAS, 341, 33

Kitzbichler M. G., White S. D. M., 2007, MNRAS, 376, 2

Kroupa P., 2001, MNRAS, 322, 231

Noeske K. G., Faber S. M., Weiner B. J. et al., 2007a, ApJ, 660, L47

Noeske K. G., Weiner B. J., Faber S. M., 2007b, ApJ, 660, L43

Panter B., Jimenez R., Heavens A. F., Charlot S., 2008, ArXiv e-prints, 0804.3091

Salim S., Charlot S., Rich R. M., Kauffmann G., 2005, ApJ, 619, L39

Salim S., Rich R. M., Charlot S., Brinchmann J., Johnson B. D., Schiminovich D., Seibert M., Mallery R., 2007, ApJS, 173, 267

Schmidt M., 1968, ApJ, 151, 393

Silk J., Rees M. J., 1998, A&A, 331, L1

Springel V., 2005, MNRAS, 364, 1105

Stringer M. J., Benson A. J., Bundy K., Ellis R. S., Quetin E. L., 2008, ArXiv e-prints, 0806.2232

Thomas D., Maraston C., Bender R., Mendes de Oliveira C., 2005, ApJ, 621, 673

van Dokkum P. G., 2008, ApJ, 674, 29

Wang J.-M., Chen Y.-M., Hu C., 2006, ApJ, 637, L85

Wang J.-M., Chen Y.-M., Yan C.-S., Hu C., Bian W.-H., 2007, ApJ, 661, L143

Weiner B. J., Papovich C., Bundy K. et al., 2007, ApJ, 660, L39

Wild V., Kauffmann G., Heckman T., Charlot S., Lemson G., Brinchmann J., Reichard T., Pasquali A., 2007, MNRAS, 381, 543

Willmer C. N. A., Faber S. M., Koo D. C., 2006, ApJ, 647, 853

Wilson J. C. et al., 2003, Proc. SPIE, 4841, 451-458

Zheng X. Z., Bell E. F., Papovich C., Wolf C., Meisenheimer K., Rix H.-W., Rieke G. H., Somerville R., 2007, ApJ, 661, L41